Late Quaternary Slip-Rate Variations along the Warm Springs Valley Fault System, Northern Walker Lane, California–Nevada Border

by Ryan Gold, Craig dePolo, Richard Briggs, Anthony Crone, and John Gosse

Abstract   The extent to which faults exhibit temporally varying slip rates has important consequences for models of fault mechanics and probabilistic seismic hazard. Here, we explore the temporal behavior of the dextral-slip Warm Springs Valley fault system, which is part of a network of closely spaced (10–20 km) faults in the northern Walker Lane (California–Nevada border). We develop a late Quaternary slip record for the fault using Quaternary mapping and high-resolution topographic data from airborne Light Distance and Ranging (LiDAR). The faulted Fort Sage alluvial fan (40.06° N, 119.99° W) is dextrally displaced 98^{+42}_{-43} m, and we estimate the age of the alluvial fan to be $41.4^{+10.0}_{-4.8}$ ka to 55.7 ± 9.2 ka, based on a terrestrial cosmogenic ^{10}Be depth profile and ^{36}Cl analyses on basalt boulders, respectively. The displacement and age constraints for the fan yield a slip rate of $1.8^{+0.8}_{-0.8}$ mm/yr to $2.4^{+1.2}_{-1.1}$ mm/yr (2σ) along the northern Warm Springs Valley fault system for the past 41.4–55.7 ka. In contrast to this longer-term slip rate, shorelines associated with the Sehoo highstand of Lake Lahontan (∼15.8 ka) adjacent to the Fort Sage fan are dextrally faulted at most 3 m, which limits a maximum post-15.8 ka slip rate to 0.2 mm/yr. These relations indicate that the post-Lahontan slip rate on the fault is only about one-tenth the longer-term (41–56 ka) average slip rate. This apparent slip-rate variation may be related to co-dependent interaction with the nearby Honey Lake fault system, which shows evidence of an accelerated period of mid-Holocene earthquakes.

Introduction

A fundamental question regarding the behavior of hazardous faults is the extent to which they experience temporal variations in slip rate at timescales significantly greater than the interval between individual earthquakes. A number of studies have demonstrated that such secular variations in slip occur along fast-moving (> 5 mm/yr) strike-slip faults located in closely spaced (20–45 km) fault networks over timescales ranging from 4 to 100 kyr, including the Marlborough fault system, New Zealand, (Knuepfer, 1992; Gold and Cowgill, 2011) and the southern San Andreas fault system, California, (Bennett *et al.*, 2004; Weldon *et al.*, 2004). Here we seek to examine such variations for slower moving (∼2 mm/yr) strike-slip faults. For these systems, high-resolution faulting chronologies are more difficult to construct owing to the longer time needed for multiple faulting events to generate appreciable offset in the face of competing processes of erosion, which degrade landforms and erase evidence of faulting (e.g., Bull, 1988; Klinger *et al.*, 2011).

In this investigation, we examine the late Quaternary slip record of the dextral Warm Springs Valley fault system (WSVFS), which is one of several en-echelon strike-slip faults in the northern Walker Lane (NWL), east of the Sierra Nevada microplate along the California–Nevada border

(Fig. 1). Other companion faults in the region include the Honey Lake and Pyramid Lake fault systems. Geodetic data indicate that the NWL accommodates ∼7 mm/yr of dextral shear motion at 39°–40° N (Dixon *et al.*, 2000; Thatcher, 2003; Hammond and Thatcher, 2007; Hammond *et al.*, 2011), which represents ∼15% of the relative plate motion between North America and the Pacific Plate (DeMets and Dixon, 1999). The WSVFS is an important study target because of sparse data regarding its Quaternary slip history and location, ∼10 km to the east of the Honey Lake fault, which has a better-defined slip history with which we can compare results. To evaluate the temporal variability in slip rate of the northern WSVFS, we focused on the Fort Sage fan site where we used airborne Light Distance and Ranging (LiDAR) data, detailed geologic mapping, and *in-situ* Terrestrial Cosmogenic Nuclide (TCN) exposure dating, to characterize the late Quaternary history of dextral slip on the northern portion of this fault system.

Geologic Framework

The anastomosing, northwest-trending WSVFS extends 96 km from the Warm Springs Valley in the south to the

Honey Lake Basin in the north and separates the Dogskin Mountains and Fort Sage Mountains on the west from the Virginia Mountains to the east (Fig. 1) (dePolo and Ramelli, 2004; dePolo, 2006). Block models used to characterize the contemporary deformation and estimate slip on faults in the NWL region are largely based on data from the Mobile Array of GPS for Nevada Transtension (MAGNET) network and the EarthScope Plate Boundary Observatory (Hammond *et al.*, 2011). A global positioning system (GPS) profile oriented 040° across the study area indicates a cumulative dextral shear-velocity gradient of ∼7 mm/yr across the NWL (fig. 4d in Hammond *et al.*, 2011), and block modeling suggests a dextral slip rate of 1.0 ± 0.3 mm/yr (95% confidence) along the WSVFS (Hammond *et al.*, 2011).

Trenching along the southern WSVFS in Warm Springs Valley (Fig. 1) has revealed evidence of eight paleoseismic events since 21 ± 4 ka (uncertainty is 2 sigma [σ] value) (dePolo and Ramelli, 2004; dePolo, 2006), but six of these
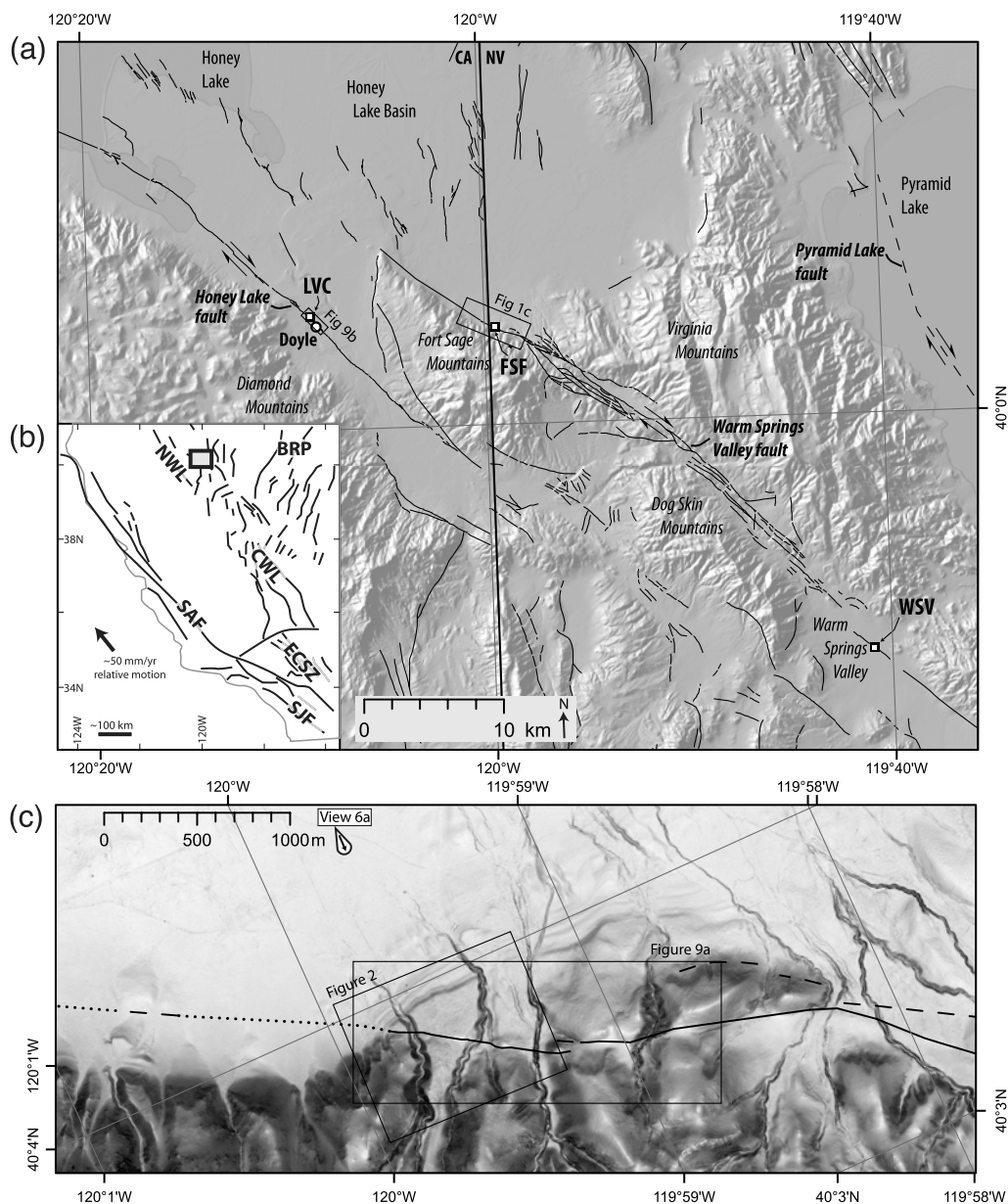

Figure 1. (a) Map showing the Honey Lake and Warm Springs Valley faults in the southern Honey Lake Basin. Abbreviations: FSF, Fort Sage fan site (subject of this paper) (dePolo, 2006); WSV, Warm Springs Valley trench site (dePolo and Ramelli, 2004; dePolo, 2006); LVC, Long Valley Creek site (Wills and Borchardt, 1993; Turner *et al.*, 2008). Quaternary faults are mapped (black lines) based on the U.S. Geological Survey Quaternary fault-and-fold database (2006) and our mapping using LiDAR data and field observations. (b) Inset map shows study area within the tectonic framework of western North America. Abbreviations: SAF, San Andreas fault; SJF, San Jacinto fault; NWL, northern Walker Lane; CWL, central Walker Lane; ECSZ, Eastern California shear zone; BRP, Basin and Range Province. (c) Overview of the northern portion of the Warm Springs Valley fault system. Underlying slopeshade image derived from airborne LiDAR data. Mapped fault (black line) is solid for high confidence, dashed for approximately located, and dotted where the fault is concealed.

events clustered between 21 ± 4 ka (luminescence age, 2σ) and 11.6 ± 1.4 cal kyr B.P. (calibrated bulk radiocarbon age, 2σ, recalibrated using OxCal, Bronk Ramsey, 2009 with the IntCal09 calibration curve, Reimer et al., 2009 from a reported bulk sample radiocarbon age of 9970 ± 550 [14]C B.P.). In contrast to this flurry of events, only two surface-rupturing events have occurred since 11.6 ± 1.4 ka. Furthermore, a buried channel deposit is right-laterally offset only 2.5 ± 0.5 m by the three most recent paleoearthquakes (dePolo and Ramelli, 2004; dePolo, 2006).

dePolo (2006) estimated a preliminary Quaternary slip rate for the WSVFS at the Fort Sage fan site, where he reported 95^{+15}_{-11} m of dextral offset recorded by the crest of the faulted alluvial fan. He qualitatively estimated an age of the fan of 50–300 ka based on an evaluation of soil development in a stream cut. These values yielded a broadly constrained slip rate of 0.3–2.2 mm/yr.

Faulds et al. (2005) and Henry et al. (2007) estimated long-term geologic slip rates on the WSVFS of 1.3–5.0 mm/yr based on dextral offsets of 8–15 km of a Miocene tuff that fills a paleovalley. Strike-slip faulting in the region initiated about 6–3 Ma, as indicated by kinematic analyses of normal and strike-slip faults in the region, ^{40}Ar/^{39}Ar geochronology of volcanic rocks and tephras, and regional correlations (Faulds et al., 2005; Henry et al., 2007; Hinz et al., 2009).

Fort Sage Fan Site, Warm Springs Valley Fault

Site Description

At our study site, the Fort Sage alluvial fan (40.06° N, 119.99° W) is cut by a single 295°-trending fault trace that extends northward away from the Fort Sage Mountains and into the Honey Lake Basin (Figs. 1 and 2). Previous mapping by Grose (1984) shows a multi-stranded fault system in the region around the Fort Sage alluvial fan. More recent Quaternary mapping by dePolo (2006) depicts a single major fault strand across the Fort Sage alluvial-fan site, although with queried secondary strands to the northeast. To evaluate potential deformation and faulting away from the trace that cuts the Fort Sage fan, we examined the geomorphology using airborne LiDAR data, aerial photographs, and field relationships. Tonal vegetation patterns and shorelines correspond with the traces mapped by Grose (1984), but we find no evidence of Quaternary faulting apart from the main strand on the Fort Sage alluvial fan.

The source material of the Fort Sage alluvial fan is from the Fort Sage Mountains, which are chiefly composed of Cretaceous granodiorite and Tertiary basalt and rhyolitic tuff (Grose, 1984). Recent Quaternary mapping identified it as a faulted fan composed of debris flows (dePolo, 2006). We divide the Fort Sage alluvial fan into three depositional elements, which include Qo2, Qo1, and Qo_{undiff}, on the basis of their convex profiles, inset relations, distinct elevations, and surface characteristics (Fig. 2). The surfaces of this suite of deposits have limited preservation of bar-and-swale topography, are covered with disaggregated and cracked boulders (maximum diameter 2–3 m), and vegetated with native shrubs. Qo2 is distinguished from Qo1 by a higher concentration of large boulders on its surface. Furthermore, Qo2 is at a higher relative elevation and has a distinct concave-up profile on the south side of the fault (Fig. 3). We excavated two pits into the Qo2 deposit to compare soil development in deposits on the opposite sides of the fault (Pit1SW and Pit2NE on Fig. 2 and in Appendix B). Importantly, soil development and the stratigraphy in the upper 40 cm of both pits are similar, which supports correlation of the Qo2 fan lobes. Inset into the eastern flank of the Qo deposits is unit Qm, an intermediate-age, low-relief alluvial deposit. Both Qo and Qm are incised (~15–25 m) by modern channels, Qa (Fig. 3).

The northern margin of the old parts of the fan (Qo2, Qo1, and Qo_{undiff}) has been trimmed by a former lake. We interpret the highest shoreline (1335 m above sea level [asl]) to have been built during the Sehoo highstand of Lake Lahontan because it exhibits a fresh morphology and is proximal to the 1334 m contour of the Lake Lahontan highstand at this locality (Adams et al., 1999). The age of this highstand is 15.8 ± 0.6 ka, determined from our calibration of the reported radiocarbon age of $13,070 \pm 60$ [14]C B.P. (Adams and Wesnousky, 1998); we recalibrated to calendar years using OxCal (Bronk Ramsey, 2009) with the IntCal09 calibration curve (Reimer et al., 2009). We map sediment from the lake, undifferentiated alluvium, wind-blown silts, and colluvium as Qy_{undiff}.

A series of younger alluvial-fan deposits (Qy3, Qy2, Qy1) have been deposited on the eastern and western flanks of the Fort Sage alluvial fan. These deposits form a thin veneer over the shorelines to the east of the Fort Sage fan. The topography of the shorelines is faintly expressed under Qy3, which indicates that Qy3 postdates the lake.

Displacement

The Fort Sage alluvial fan is right-laterally faulted. The fact that the morphology of the fan is subdued as a result of post-depositional processes such as erosion, landslides (Qls), and stream incision (Qm, Qy3-1) limits our ability to confidently reconstruct the landform with small displacement uncertainty. We follow previous efforts, such as at the Biskra Palms site along the San Andreas fault (Behr et al., 2010) and the Furnace Creek alluvial-fan site along the Death Valley–Fish Lake Valley fault system (Frankel et al., 2007), and identify the Qo2 fan axial crest on opposite sides of the fault to estimate lateral displacement of the fan. The topographic profiles (Fig. 3a,b) and a slope-aspect map (Fig. 4) show the inflection associated with the Qo2 axial crest. South of the fault, the axial crest is evident in the Qo2 fan lobe, especially ~40–50 m south of the fault. However, on the north side of the fault the axial fan crest is less obvious because the Qo2 and Qo1 fan lobes are at similar elevations. Topographic
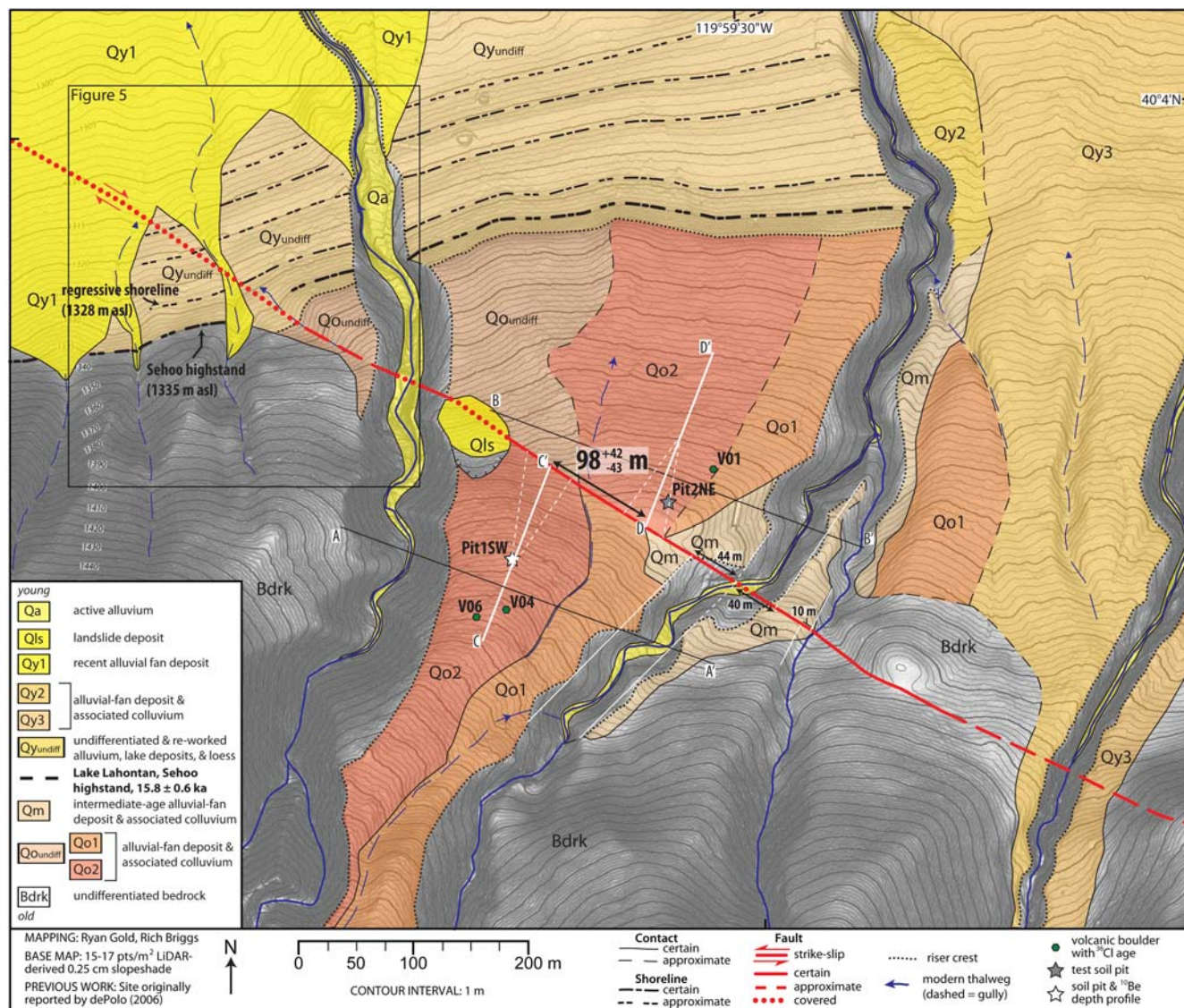
Figure 2. Topographic and surficial geologic map of the Fort Sage alluvial-fan site. Mapping and contours are overlain on slopeshade map derived from the airborne LiDAR data. At the site, the axial crest of a north-sloping Qo2 fan is right-laterally offset 98^{+42}_{-43} m by the Warm Springs Valley fault. Shorelines associated with the Sehoo highstand of Lake Lahontan are not significantly laterally offset by faulting. Additional offset channel margins are indicated. Fault parallel (A–A′ and B–B′) and fault perpendicular (C–C′ and D–D′) are presented in Figure 3. The color version of this figure is available only in the electronic edition.

profile B–B′ (Fig. 3b) shows the Qo2 fan lobe north of the fault, which is separated from Qo1 to the east by a small swale. Reconstructing the Qo2 axial fan crest yields a preferred dextral offset of 98 m (Fig. 4b,d). This reconstruction also aligns a bedrock margin, east of the fan complex (Fig. 4d).

While the preferred reconstruction best satisfies our field observations, ambiguities in cross-fault surface correlations and in the precision of mapped contacts (e.g., Qo1–Qo2 contact, north of fault) lead us to conservatively characterize the uncertainty in fan's dextral offset (Fig. 4e,f). The minimum displacement reconstruction (55 m) aligns the channel on the east flank of the fan and an inflection line on the Qo-fan complex (Fig. 4e). This model allows for the possibility that the

entire convex-up lobe, north of the fault, is Qo2. In this model, Qo1 and Qm are inset into Qo2 on the east and faulting does not occur until the stream channel east of the fan has incised Qo2, Qo1, and Qm. The maximum displacement reconstruction (140 m) adopts an alternative projection of the Qo2 fan axial crest and aligns the western margin of the Qo2 fan surface south of the fault with the Qo2/Qoundiff contact north of the fault.

In summary, the preferred (98 m), minimum (55 m), and maximum (140 m) reconstructions yield a right-lateral displacement of 98^{+42}_{-43} m since deposition of Qo2 (Fig. 4). The assigned uncertainty is sufficiently conservative to be equivalent to plus or minus the $2-\sigma$ confidence level. Our measurements overlap with and have broader uncertainty
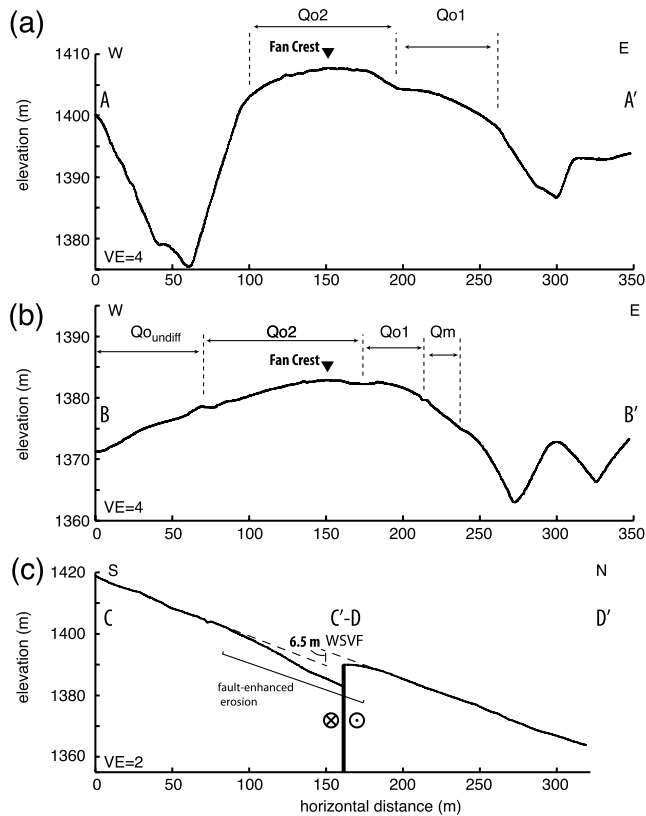
Figure 3. Fault-parallel topographic profiles measured from airborne LiDAR-derived digital elevation model (a) south of fault and (b) north of fault with Qo2 fan axial crest indicated by inverted triangle. (c) Fault-perpendicular profile measured along fan-axial crest, indicating 6.5 m of up-to-the-north vertical displacement across the Warm Springs Valley fault (WSVF). Profile locations are indicated in Figure 2.

than the 95^{+15}_{-11} m measurement reported by dePolo (2006).

In addition to the Qo2 fan-crest offset, we note that projections of the margins of the stream channel incised into the Qm deposit on the eastern margin of the fan suggest an apparent right-lateral deflection of 40–44 m (Fig. 2). Furthermore, the western channel margin of a small channel, west of the Fort Sage fan, shows an apparent right-lateral deflection of ∼10 m.

The intersection of the fault trace with regressive shorelines of pluvial Lake Lahontan provides important constraints on the fault's slip history. The precise position of the fault northwest of the Qo deposits is difficult to definitively determine because the fault is obscured by young alluvium, colluvium, and loess. Figure 5 illustrates a range of fault projections in this region and highlights a possible tectonic lineament among the shorelines. Despite the subtle geomorphology in the area of this intersection, the shorelines do not show any observable dextral or vertical offset where the fault projects across them. In detail, the fault trace intersects the highest shoreline (presumably from the Sehoo highstand of Lake Lahontan) northwest of the Qo deposits. Unfortunately,

two small gullies merge in this locality, which complicates our ability to resolve possible lateral offsets of the shoreline. As a result, we must rely on projections of the shoreline across the fault. While the gullies prevent us from definitively determining if the shoreline is laterally displaced, we can conclude that if it is displaced, the total dextral displacement is no more than 3 m. A series of topographically lower regressional shorelines at 1328 m, 1320 m, and 1316 m asl cross the fault's projection to the west-northwest of the highest shoreline and these shorelines are aligned across the gullies, maintain constant elevation, and also appear unfaulted. Another possibility is that the fault does not continue northwest into the Honey Lake basin, but instead steps westward and does not intersect with the shorelines. However, even if this alternative interpretation is correct, previous mapping (Wills, 1990) and our reconnaissance field observations indicate that the range-front bounding fault northwest of the study site has not experienced post-Lahontan faulting because shorelines and alluvial fans are uninterrupted along the range front. Based on these observations, we conclude that the regressional and Sehoo highstand shorelines cannot be laterally offset more than 3 m.

Finally, we consider vertical fault motion. In particular, we note that the Qo2 axial fan crest shows a vertical component of north-side-up faulting. Two topographic profiles measured along the preferred Qo2 axial crest, (south of fault, C–C′; north of fault, D–D′) resolve a vertical offset of 6.5 m, after the near-field portions of the profiles are removed because they are affected by near-field fault-related erosion, (Fig. 3c). The amount of vertical motion is ∼7% of the (preferred) horizontal faulting. We postulate that vertical faulting may result from contraction associated with either the small left step in the Warm Springs Valley fault (Fig. 1b) or the more regional left step between the overlapping and right slipping Honey Lake and Warm Springs Valley faults (Fig. 1a).

Geochronology

We measured concentrations of the *in-situ* Terrestrial Cosmogenic Nuclides (TCNs) [10]Be and [36]Cl to establish the depositional age of the Qo2 lobe of the Fort Sage alluvial fan (Tables 1–4 and Figs. 6, 7). TCNs are produced via secondary interactions of cosmic rays with minerals in target materials (Gosse and Phillips, 2001), and the concentration of these nuclides can be used to estimate the age and geomorphic history of a landform. However, for deposits such as alluvial fans, samples can contain an inherited amount of the target nuclide. A depth profile, which relies on multiple subsurface samples of amalgamated sands from different depths below the fan surface, can be used to estimate the inherited components (Anderson *et al.*, 1996; Repka *et al.*, 1997; Hancock *et al.*, 1999) provided that the average inheritance is constant over the range of depth. To determine the depositional age of the Fort Sage fan, we rely on surface-exposure dating from a [10]Be depth profile using coarse
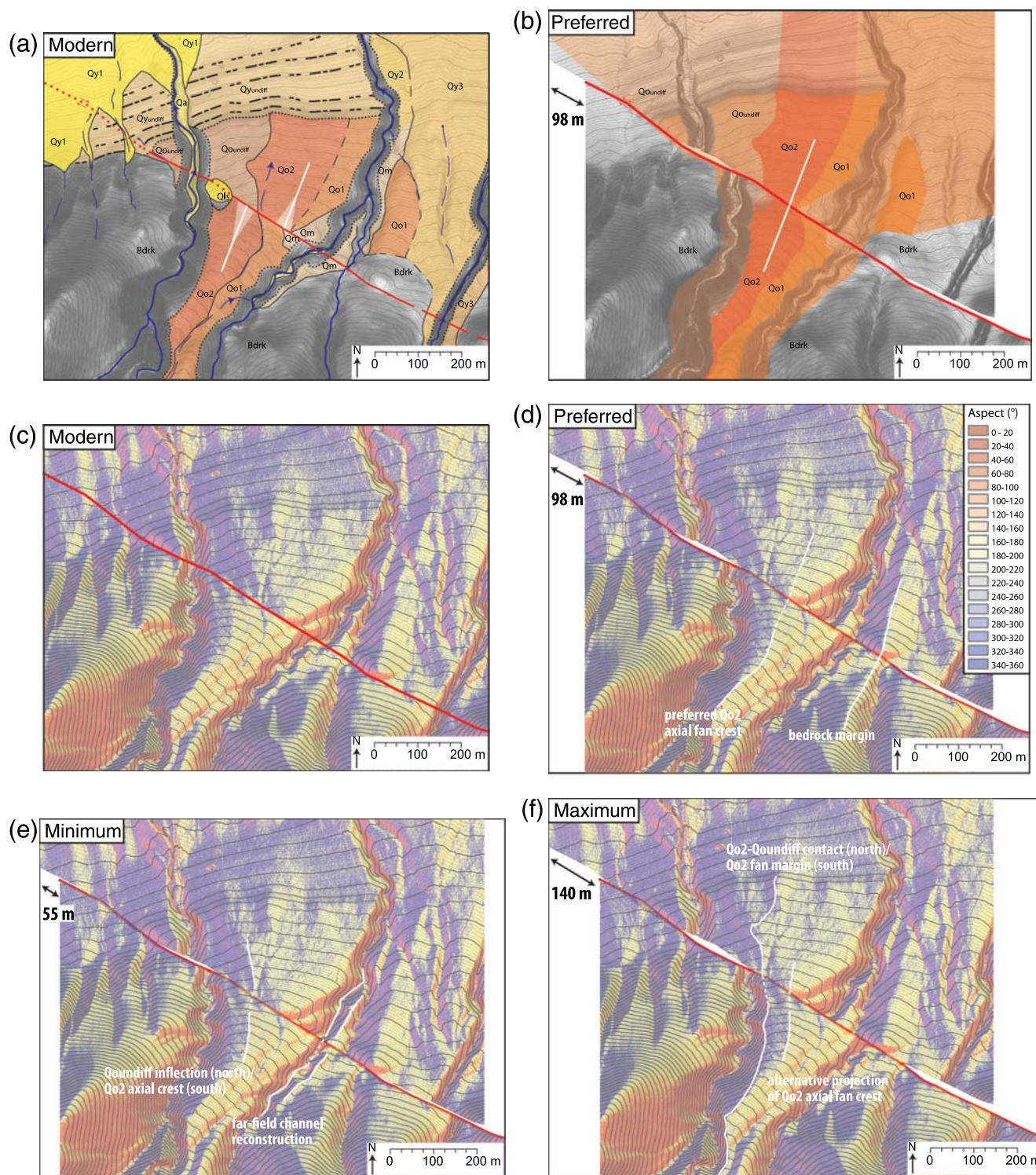
Figure 4. Reconstruction of the Fort Sage fan site. (a) Modern configuration and (b) preferred reconstruction with surficial geologic mapping. Slope aspect map derived from the airborne LiDAR data for (c) modern configuration, (d) preferred reconstruction, (e) minimum offset, and (f) maximum offset. Reconstructed features are indicated by white lines and discussed in main text. Contour interval is 1 m. The color version of this figure is available only in the electronic edition.

(350–500 μm and 500–1000 μm) quartz-rich sand from a soil pit in the faulted fan and ^{36}Cl analyses on volcanic boulders on the Qo2 surface. The sampled boulders are part of the same depositional package as the sampled sand fraction (Fig. 7), and we therefore expected compatible geochronologic results.
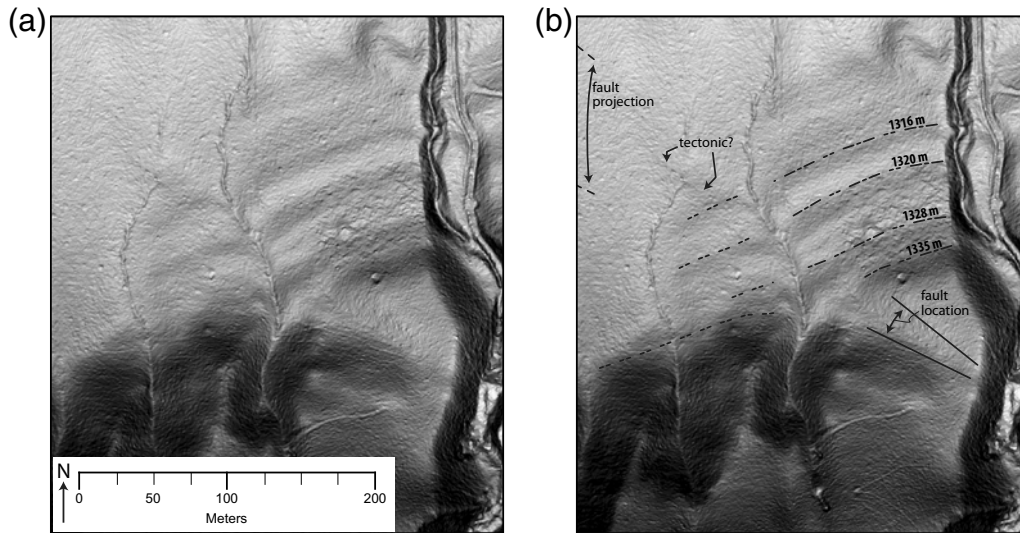
Figure 5. (a) Uninterpreted and (b) interpreted slopeshade map of the Warm Springs Valley fault intersection with Sehoo highstand shorelines from Lake Lahontan. The shorelines are not detectably offset by the fault trace where it projects across the basin, which indicates minimal lateral offset since 15.8 ka. Symbology in (b) follows legend in Figure 2.

Our four-sample *in-situ* ^{10}Be depth profile was collected from Pit1SW, which is located south and upslope of the fault trace (Figs. 2 and 7; see Appendix C for details of the samples and analysis). We modeled the depositional age of the Qo2 alluvial fan to discriminate the inherited TCN component from the post-depositional TCN component using a depth-profile calculator that uses a Monte Carlo simulation (Hidy *et al.*, 2010; see Table 2). The Monte Carlo analysis indicates the depositional age of Qo2 to be $41.4^{+10.0}_{-4.8}$ ka (2σ) (Fig. 7c–f). In contrast, the concentrations of *in-situ* TCN ^{36}Cl from three basalt boulders on the Qo2 surface yielded a spread of ages ranging from 55.7 to 176.9 ka (Fig. 6b–d, Table 3, see Appendix D for details), which are systematically older than the ^{10}Be result. However, the youngest ^{36}Cl boulder age from V04 of 55.7 ± 9.4 ka (2σ) overlaps within error with the ^{10}Be depth profile age.

Based on the following discussion focused on predepositional inheritance and post-depositional erosion, we consider the ^{10}Be depth profile age and youngest ^{36}Cl age to provide the most reliable indication of timing of deposition of the Qo2 fan deposit. A key advantage of the ^{10}Be depth profile model is that it resolves both the Qo2 deposit's depositional age (adjusting for net aggradation or erosion) and the inherited ^{10}Be concentration. This analysis indicates negligible inheritance for the quartz-sand fraction and minimal surface erosion.

In contrast, given the small sample population ($n = 3$) of ^{36}Cl surface-exposure ages for boulders, it is difficult to use statistical tests to distinguish inheritance or erosional processes. However, the large spread in ^{36}Cl ages (55.7–176.9 ka) may indicate a significant inherited component of ^{36}Cl or post-depositional erosion of the boulder surfaces in some portion of the sample population. Inheritance would tend to lead to an overestimate of fan age, favoring the

youngest ^{36}Cl boulder age. Post-depositional erosion is a more complex process. Thermal neutron loss to air and rock moisture results in a ^{36}Cl concentration that initially increases with depth before decreasing exponentially. Thus a small amount of boulder surface erosion, as may be indicated by cracking and evidential weather of the boulder surfaces, would cause the unadjusted ^{36}Cl exposure age to overestimate the actual exposure age. For these reasons and because of its overlap within error with the ^{10}Be depth profile age, we think that from the boulder population, the youngest ^{36}Cl boulder age most closely approximates the depositional age of Qo2. In summary, we propose that the ^{10}Be depth profile and youngest ^{36}Cl-dated boulder are best considered together and suggest that the Qo2 lobe of the Fort Sage fan was deposited between $41.4^{+10.0}_{-4.8}$ ka and 55.7 ± 9.2 ka.

A final argument in support of the 41.4–55.7 ka depositional age of the Fort Sage fan is that it broadly correlates to an interval of regional fan alluviation. For example, in Smith Valley, Nevada, Wesnousky and Caffee (2011) document the age of fan alluviation as 60.5 ± 10 ka ($1 - \sigma$ error converted to $2 - \sigma$ value). Along George Creek near Owens Valley, California, Le *et al.* (2007) report a fan surface age of 60.9 ± 13.2 ka ($1 - \sigma$ error converted to $2 - \sigma$ value). Lee *et al.* (2009) report a fan surface age of 53.6 ± 1.2 ka in the Queens Canyon area, south of the Mina deflection. Along the Eastgate fault in central Nevada, Crone *et al.* (2005) report a fan age of 59.2 ± 5.5 ka. Finally, the age spans the lower limit of the qualitative age range suggested by dePolo (2006) for this site of 50–300 ka based on soil development.

Late Quaternary Reconstruction and Slip Rates

The Qo2 fan lobe has 98^{+42}_{-43} m of right-lateral offset by the WSVFS whereas the shorelines associated with the

Table 1

^{10}Be AMS Analyses from the Fort Sage Fan Site

Sample Name	Latitude* (°N)	Longitude* (°E)	Altitude* (m)	Topographic Shielding Factor	Surface Spallogenic Production Rate† (atoms/g/yr)	Depth‡ (cm)	Quartz Mass (g)	Mass Carrier Solution§ (g)	^{10}Be/^{9}Be Corrected for Blank and Boron	^{10}Be/^{9}Be Error	^{10}Be Concentration (atoms/g SiO$_2$)	AMS ±‖	%
FTSage37cm	40.06329	118.99435	1404	0.99598	13.1	37	34.5400	0.3033	5.60199×10^{-13}	9.19923×10^{-15}	442364	8665	2.80%
FTSage46cm	40.06329	118.99435	1404	0.99598	13.1	46	50.1242	0.3098	6.85435×10^{-13}	1.27851×10^{-14}	381408	8165	2.93%
FTSage74cm	40.06329	118.99435	1404	0.99598	13.1	74	50.4197	0.3122	4.75695×10^{-13}	8.15585×10^{-15}	264659	5372	2.85%
FTSage86cm	40.06329	118.99435	1404	0.99598	13.1	86	50.1316	0.3058	4.44377×10^{-13}	8.29521×10^{-15}	243408	5278	2.95%

Error#

*Latitude, longitude, and altitude determined from handheld GPS unit.

†Production rate calculated using Monte Carlo calculator (Hidy et al., 2010) based on Stone (2000) after Lal (1991).

‡Depth measured to the middle of stratigraphic interval from which sand was collected. Sand was collected within intervals ±3 cm from reported depth.

§Carrier concentration 1354 μg/ml.

‖Concentration error (1 − σ) from AMS.

#Error associated with AMS, plus additional 2% error added in quadrature from sample preparation from Gosse and Phillips (2001).

Table 2
^{10}Be Depth Profile Monte Carlo Results

	Age (ka)	Inheritance (10^4 atoms/g)	Erosion Rate (cm/ka)
Mean	44.0	2.91	−0.12
Median	43.7	2.57	−0.09
Mode	43.3	0.74	0.31
Minimum $\chi2$	43.3	3.52	−0.09
Maximum	59.9	11.95	0.59
Minimum	30.2	0	−0.94
Bayesian most probable*	41.4	0	0.35
Bayesian 2-sigma upper	51.4	7.17	0.37
Bayesian 2-sigma lower	36.6	0.11	−0.72

*Bayesian most probable age is interpreted to represent the best model age for the Qo2 surface.

Sehoo highstand and subsequent regression are unfaulted or laterally offset less than 3 m. These relationships allow us to calculate independent average slip rates since 41.4–55.7 ka for the Qo2 fan lobe and since 15.8 ka after the Sehoo highstand. Furthermore, we construct a fault-slip history with interim slip rates over the interval between deposition of these features (Fig. 8a).

We calculate an average slip rate of $1.8^{+0.8}_{-0.8}$ mm/yr to $2.4^{+1.2}_{-1.1}$ mm/yr (2σ) since deposition of the laterally offset Qo2 Fort Sage alluvial fan (98^{+42}_{-43} m [2σ] with the ^{36}Cl age of 55.7 ± 9.2 ka and ^{10}Be age of $41.4^{+10.0}_{-4.8}$ ka [2σ], respectively). Uncertainties are determined by propagating the age and displacement uncertainties in quadrature. Our rate is within the 0.3–2.2 mm/yr range reported by dePolo (2006) based on his reconnaissance study here, and within the 3–6 Ma, long-term rate of 1.3–5.0 mm/yr based on geological data (Faulds *et al.*, 2005; Henry *et al.*, 2007; Hinz *et al.*, 2009). The lower bound of our estimate also overlaps (at 2σ) with the rate of 1.0 ± 0.3 mm/yr of dextral slip based on the block model of GPS measurements (Hammond *et al.*, 2011).

Our field mapping and previous mapping efforts (Wills, 1990) indicate that the WSVFS has not significantly offset Sehoo-age, highstand shorelines of Lake Lahontan (Figs. 2 and 5). If the fault maintained a constant slip rate of about 2 mm/yr since the shorelines formed about 15.8 ± 0.6 ka, then we would expect that the shorelines would be displaced ∼31.6 m. It is clear that the shorelines cannot be offset more than 3 m, limiting the post-15.8 ka slip rate on the fault to ≤0.2 mm/yr (3 m with the Sehoo-highstand age 15.8±

0.6 ka), which is one-tenth the average, post-Qo2 slip rate. This suggests that the slip rate since 15.8 ka has decreased dramatically, relative to the longer-term rate of strain release in the past 41–56 kyr.

The two strain markers (offset fan and unfaulted shorelines) yield an interim slip rate of $2.5^{+1.2}_{-1.2}$ mm/yr to $3.8^{+1.8}_{-2.3}$ mm/yr (2σ) from 41.4–55.7 ka to 15.8 ka, and a post-15.8 ka slip rate of <0.2 mm/yr (Fig. 8a). The interim slip-rate calculation is made by combining the fan-offset value (98^{+42}_{-43} m) with the interval between the Qo2 fan age of 55.7 ± 9.2 ka to $41.4^{+10.0}_{-4.8}$ ka and the Lake Lahontan Sehoo highstand (15.8 ± 0.6 ka). Uncertainties are propagated in quadrature. We note that the lowest possible slip rate between the Qo2 and Lahontan shorelines at the $2 - \sigma$ extreme (minimum offset, maximum age) is 1.2 mm/yr, which is still many times greater than the post-Sehoo-highstand slip rate of <0.2 mm/yr.

Discussion

Our interpretation of a sharp decrease in the post-15.8 ka slip rate for the WSVFS, which is based on geomorphic and geochronologic observations, closely agrees with preliminary paleoearthquake recurrence information reported elsewhere along the fault system. Along the southern WSVFS, dePolo (2006) and dePolo and Ramelli (2004) report evidence of four surface-faulting events in the ∼5 kyr-interval immediately prior to the Lahontan highstand, followed by only two events in the ∼4 kyr interval following the highstand (Fig. 8b). Since the highstand at 15.8 ± 0.6 ka, relationships observed in their trenches suggest that only 2.5 ± 0.5 m of dextral displacement has occurred. Furthermore, since 11.6 ka, they report evidence of only two ruptures, with the most recent event being minor and lacking evidence of lateral offset. Thus, available trench evidence suggests a sharp decrease in dextral slip at both the Fort Sage fan and Warm Springs Valley sites since the Sehoo highstand. Given that these sites are at the northern and southern ends of the WSVFS, we infer that the entire fault system has had a post-Lahontan slip rate that is substantially less than the average rate over the preceding 25–40 kyr.

Regional strain rates in the NWL are driven by plate-boundary forces (e.g., Thatcher *et al.*, 1999; Wesnousky, 2005), and we find no basis for expecting that those plate-scale forces have changed in the past 50 kyr. If the

Table 3
^{36}Cl AMS Analyses from the Fort Sage Fan Site

Sample Name	Latitude* (°N)	Longitude* (°E)	Altitude* (m)	Topographic Shielding Factor	Rm (^{36}Cl/10^{15} Atoms of Cl) (ratio)	Cl (ppm)	Age (ka)	2σ Age Uncertainty (ka)
09WSVF-FtSageN-V01	40.06384232	−119.9923094	1380	1	3295.8813	49.4083	176.9	24.1
10WSVF-FTSageS-V04	40.06340655	−119.9943586	1400	1	1968.5102	29.2899	55.7	9.2
10WSVF-FTSageS-V06	40.06289056	−119.994851	1413	1	3872.6211	32.2356	130.3	16.7

*Latitude, longitude, and altitude determined from handheld GPS unit.

Table 4
Fort Sage Fan Site ^{36}Cl Chemical Data

Sample Name	LOI* (%)	H$_2$O in LOI* (%)	Na$_2$O (%)	MgO (%)	Al$_2$O$_3$ (%)	SiO$_2$ (%)	P$_2$O$_5$ (%)	K$_2$O (%)	CaO (%)	TiO$_2$ (%)	MnO$_2$ (%)	Fe$_2$O$_3$ (%)	Cl (ppm)	B (ppm)	Sm (ppm)	Gd (ppm)	U (ppm)	Th (ppm)	Cr (ppm)	Li (ppm)
09WSVF-FtSageN-V01	4.76	78.93	2.80	2.31	17.63	56.48	0.02	2.06	6.25	1.08	0.07	6.55	NaN	30	2.3	2.3	2.24	4.4	0	20
10WSVF-FTSageS-V04	4.76	79.00	2.82	2.32	17.55	56.44	0.01	2.12	6.24	1.08	0.09	6.57	NaN	20	1.9	2.1	2.19	4	0	20
10WSVF-FTSageS-V06	4.75	78.99	2.81	2.46	17.47	56.68	0.02	2.11	6.24	1.08	0.08	6.32	NaN	30	1.9	2.06	2.21	4.2	0.01	20

*LOI is loss on ignition.

(a)

(b)

V01: 176.9 ± 24.1 ka

(c)

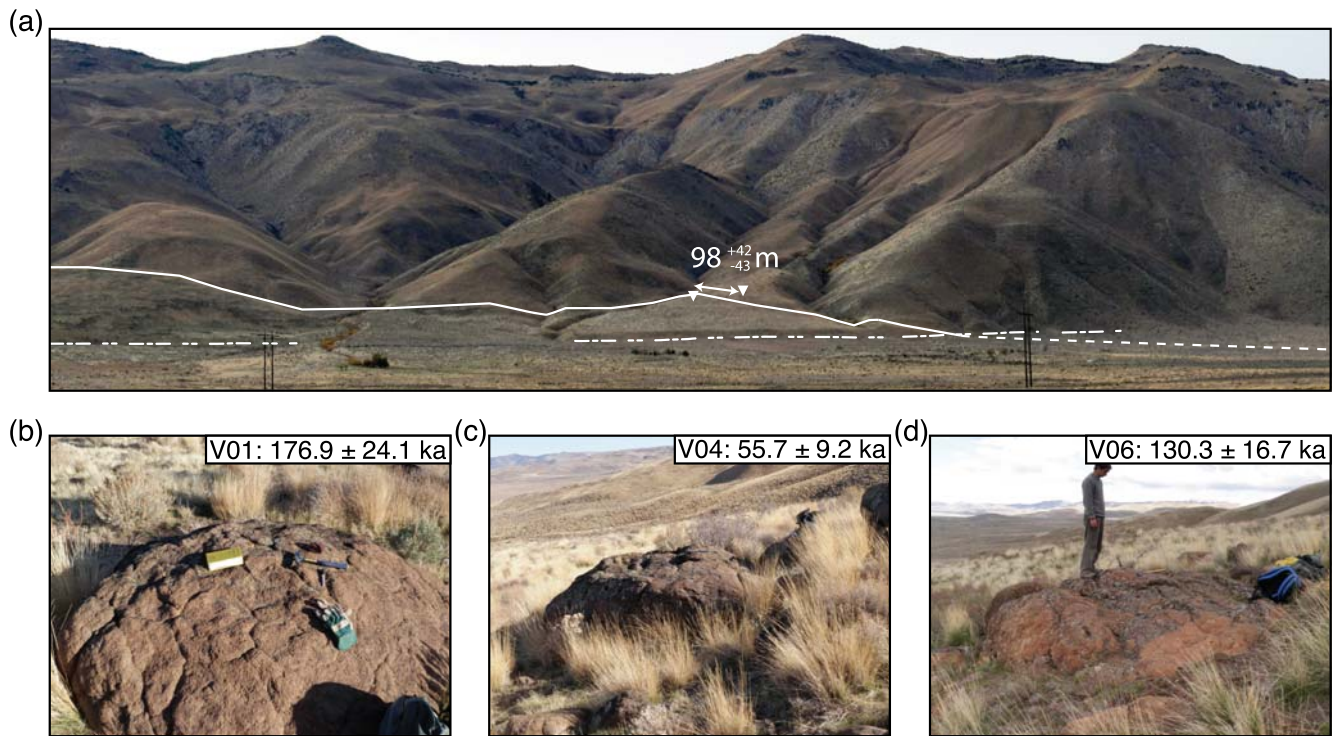
V04: 55.7 ± 9.2 ka

(d)

V06: 130.3 ± 16.7 ka

Figure 6. Photographs of the Fort Sage fan site. (a) Overview image of the site, looking west with the Fort Sage Mountains in the background; the fault is indicated by solid and dashed white line, the Sehoo shoreline by alternating double short and long dashed white line, and the fan crest by inverted triangles. Basalt boulders sampled for ^{36}Cl analysis (b) V01, (c) V04, and (d) V06. Locations for basalt boulders are shown on site map in Figure 2. The color version of this figure is available only in the electronic edition.

post-Lahontan slip rate on the WSVFS is only about one-tenth the longer-term rate, then is there evidence that other nearby faults may have increased post-Lahontan slips to balance the regional rate? A likely candidate is the Honey Lake fault, which is only about 10 km away from, and overlaps with the WSVFS (Fig. 1). Two studies of the Honey Lake fault have reported slip rates at Long Valley Creek, where faulting has dextrally displaced a Holocene terrace riser. Wills and Borchardt (1993) and Turner *et al.* (2008) report essentially identical slip rates of 1.1–2.6 mm/yr and 1.7 ± 0.6 mm/yr, respectively. Paleoseismic investigations at this site also document evidence of at least four post-7.0 ka surface-rupturing events, with three events clustering between 7.0 and 4.7 ka (Fig. 8b) (Wills and Borchardt, 1993; Turner *et al.*, 2008). Unfortunately, the paleoseismic record for the Honey Lake fault does not extend beyond the mid-Holocene or as far back as the Warm Springs Valley record, but it is noteworthy that the mid-Holocene earthquake cluster along the Honey Lake fault occurred during the middle of the period of reduced slip on the WSVFS.

A comparison of the WSVFS and Honey Lake fault morphologies shows a marked difference in the freshness of the fault scarp and supports the paleoseismic records indicating more recent faulting along the Honey Lake fault (Fig. 9). We speculate that the Honey Lake fault system and WSVFS may have slipped in complementary ways such that a period of clustered earthquake activity on one fault corresponds to a quiescent period on the other; however, the data are insuffi-

cient to test this hypothesis. Furthermore, we suggest that the overlapping geometry of these faults and minor heterogeneities within the Fort Sage Mountains between them may be a factor that allows the regional strain to be released in an oscillating pattern between the faults. Such anti-correlated behavior has been proposed or observed at a variety of timescales between the strike-slip Anatolian faults (Ambraseys, 1971; Hubert-Ferrari *et al.*, 2003), normal faults in the Taupo Rift (Nicol *et al.*, 2006), and the San Andreas and San Jacinto faults (Bennett *et al.*, 2004).

Finally, we consider the seismic hazard posed by the WSVFS and whether a long-term (late Quaternary) slip rate (10 s of kyr) or the more recent record of the last few thousand years is more representative of the fault's near-term earthquake potential. The relatively high longer-term slip rate of 1.8–2.4 mm/yr versus the apparent post-15.8 ka of <0.2 mm/yr, in conjunction with the generally subdued geomorphic expression of the fault, might lead to the expectation that a surface-rupturing earthquake is overdue. However, the longer recurrence of earthquakes since 15.8 ka suggests a much lower hazard. If the Honey Lake or some other nearby fault is now where most of the regional strain is being released, then the likelihood of a future rupture on the WSVFS may be significantly lower than on adjacent faults. Results from regional geodetic block models (Hammond *et al.*, 2011), which report an intermediate slip rate of 1.0 ± 0.3 mm/yr along the WSVFS, suggest that strain is accumulating on the WSVFS and that it is not clearly in a quiescent
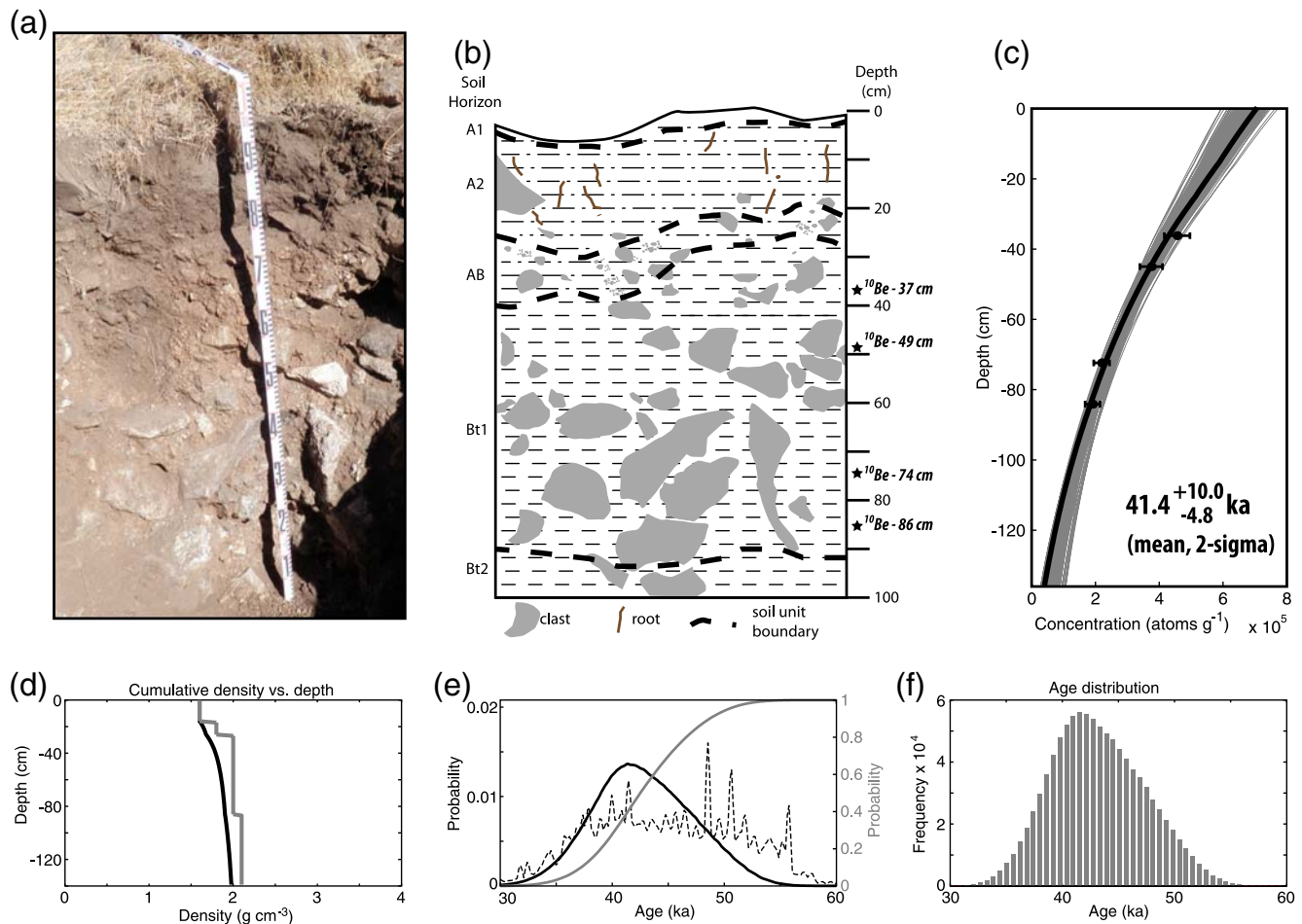
Figure 7. (a) Photograph of southern wall of Pit1SW excavation in Qo2 deposit (location shown on Fig. 2). (b) Simplified log of deposits and soil development in Pit1SW; locations of amalgamated sands collected for ^{10}Be depth profile are indicated by stars. (c) The ^{10}Be depth profile Monte Carlo model results. The black curve represents the age-erosion-inheritance scenario with the lowest χ^2 fit of the data. The gray curves are all 1,000,000 scenarios fitting within the 2σ error of each measured concentration. (d) Bulk density of the section. The gray curve is measured and the black curve is the integrated cumulative-bulk density used in the model. (e) Age results from the depth profile. The smoothed χ^2 (dashed curve), probability density function (black), and cumulative distribution functions (gray curve) for the depositional age (output from Hidy *et al.*, 2010 version 2.1). (f) The frequency distribution of the ages is from 1,000,000 scenarios. The color version of this figure is available only in the electronic edition.

period. This discrepancy highlights important unresolved issues in probabilistic seismic-hazard analyses (e.g., Petersen *et al.*, 2008): Are recent earthquake clusters or periods of recent quiescence more important for predicting future hazard? Do geodetic data provide the necessary information for discriminating between these two alternatives?

Conclusion

Analysis of airborne LiDAR data combined with TCN dating indicate that the Fort Sage alluvial fan has a preferred dextral displacement of 98^{+42}_{-43} m across the WSVFS. The fan has a depositional age of $41.4^{+10.0}_{-4.8}$ ka to 55.7 ± 9.2 ka. The combination of this offset and age yields an average late Quaternary slip rate of $1.8^{+0.8}_{-0.8}$ mm/yr to $2.4^{+1.2}_{-1.1}$ mm/yr (2σ). In contrast, where the fault crosses nearby Sehoo-age highstand shorelines of pluvial Lake Lahontan, the shorelines are either unfaulted or are, at most, offset 3 m. This indicates

that, at most, the latest Quaternary slip rate is 0.2 mm/yr since 15.8 ± 0.6 ka. Together, these data suggest that since 15.8 ka, the slip rate on WSVFS has been at most only one-tenth the late Quaternary average slip rate.

We speculate that this variable slip rate may be related to possible interaction and oscillating slip with the nearby Honey Lake fault. Limited data on the paleoseismic history of both faults, as well as qualitative geomorphic observations, suggests that the WSVFS had a period of high activity between 21 and 11.6 ka, and since that time has experienced one or perhaps two surface-rupturing earthquakes. In contrast, the Honey Lake fault has paleoseismic evidence of a cluster of mid-Holocene earthquakes between 7.0 and 4.7 ka, accompanied by a clear geomorphic expression of recent surface rupture. The possibility of interactions between these closely spaced (10–20 km), largely overlapping, and slow-moving (~2 mm/yr) strike-slip faults can be tested by obtaining longer slip records on the Honey Lake fault.
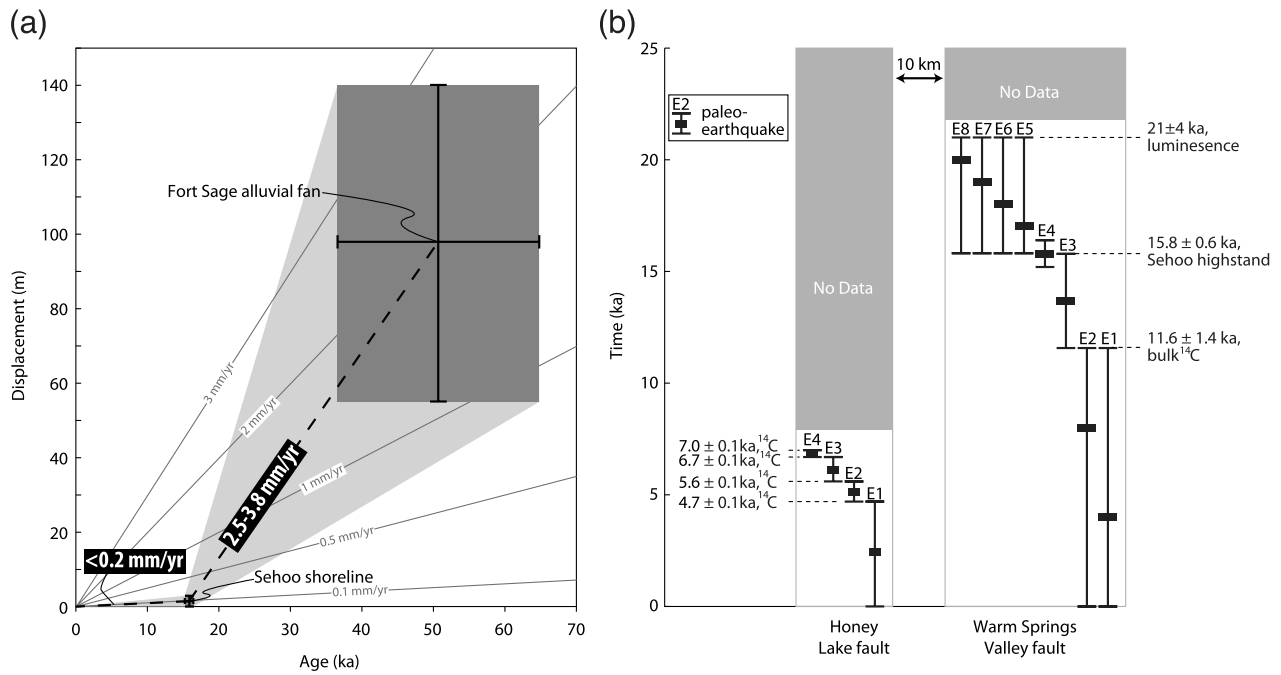
Figure 8. (a) The slip history constructed from offset landforms at the Fort Sage fan site. (b) Paleoseismic records for the Honey Lake and Warm Springs Valley fault systems, determined at the Long Valley Creek and Warm Springs Valley sites, respectively. The sources of information are Turner *et al.* (2008) for the Honey Lake fault and dePolo and Ramelli (2004) and dePolo (2006) for the Warm Springs Valley fault system. The age control and sample type are indicated.
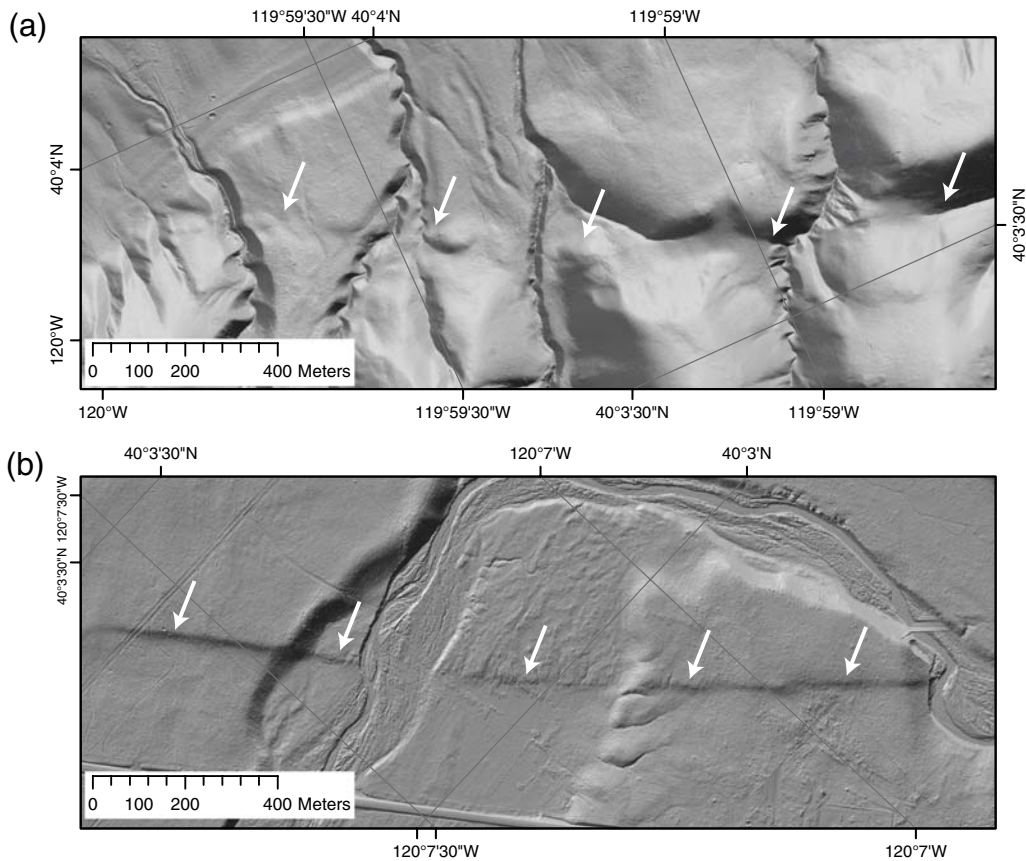

Figure 9. Comparison of the fault morphology (white arrows) along the (a) Warm Springs Valley fault system and (b) Honey Lake fault. The freshness of the fault scarp along the Honey Lake fault indicates more recent surface-rupturing earthquakes along this fault system. Base maps shown at the same scale and derived from airborne LiDAR data of the same resolution. Map locations are shown on Figure 1.

Data and Resources

The airborne Light Distance and Ranging (LiDAR) data presented in this paper are publically available from Open-Topography (http://www.opentopography.org, last accessed August 2012). The National Earthquake Hazard Reduction Program (NEHRP) technical reports reference in this study (dePolo and Ramelli, 2004; dePolo, 2006) were accessed from the USGS External Research website (http://earthquake.usgs.gov/research/external/research.php, last accessed August 2012). The online Cronus ³⁶Cl Exposure Age calculator used to calculate boulder exposure ages is accessible at: http://www.cronuscalculators.nmt.edu/calcs/cl-36/ (last accessed May 2012).

References

Adams, K. D., and S. G. Wesnousky (1998). Shoreline processes and the age of the Lake Lahontan highstand in the Jessup embayment, Nevada, *Bull. Geol. Soc. Am.* **110,** 1318–1332.

Adams, K. D., S. G. Wesnousky, and B. G. Bills (1999). Isostatic rebound, active faulting, and potential geomorphic effects in the Lake Lahontan basin, Nevada and California, *Bull. Geol. Soc. Am.* **111,** 1739–1756.

Ambraseys, N. (1971). Value of historical record of earthquakes, *Nature* **232,** 375–379.

Anderson, R. S., J. L. Repka, and G. S. Dick (1996). Explicit treatment of inheritance in dating depositional surfaces using in situ ¹⁰Be and ²⁶Al, *Geology* **24,** 47–51.

Balco, G., J. Stone, N. Lifton, and T. Dunai (2008). A complete and easily accessible means of calculating surface exposure ages or erosion rates from ¹⁰Be and ²⁶Al measurements, *Quaternary Geochronol.* **3,** 174–195.

Behr, W. M., D. H. Rood, K. E. Fletcher, N. Guzman, R. Finkel, T. C. Hanks, K. W. Hudnut, K. J. Kendrick, J. P. Platt, R. J. Sharp, R. J. Weldon, and J. D. Yule (2010). Uncertainties in slip-rate estimates for the Mission Creek strand of the southern San Andreas fault at Biskra Palms Oasis, southern California, *Bull. Geol. Soc. Am.* **122,** 1360–1377.

Bennett, R. A., A. M. Friedrich, and K. P. Furlong (2004). Codependent histories of the San Andreas and San Jacinto fault zones from inversion of fault displacement rates, *Geology* **32,** 961–964.

Bronk Ramsey, C. (2009). Bayesian analysis of radiocarbon dates, *Radiocarbon* **51,** 337–360.

Bull, W. B. (1988). Relative rates of long-term uplift of mountain fronts, in *Directions in Paleoseismology: Proceedings of Conference XXXIX,* A. J. Crone and E. M. Omdahl (Editors), *U. S. Geological Survey National Earthquakes-Hazards Reduction Program Open-File Rept.* 87-673, 192–202.

Crone, A. J., J.-B. Kyung, M. N. Machette, D. J. Lidke, K. Okumura, and S. A. Mahan (2005). Data related to late Quaternary surface faulting on the Eastgate fault, Churchill County, Nevada, *USGS Scientific Investigations Map-2893,* scale 1:75,000.

DeMets, C., and T. Dixon (1999). New kinematic models for Pacific-North America motion from 3 Ma to present; I, Evidence for steady motion and biases in the NUVEL-1A model, *Geophys. Res. Lett.* **26,** 1921–1924.

dePolo, C. M. (2006). Determination of fault slip rates, paleoearthquake history, and segmentation of the Warm Springs Valley fault system, *NEHRP Technical Report, 04HQGR0082,* 35 pp.

dePolo, C. M., and A. R. Ramelli (2004). Paleoseismic studies along the Warm Springs Valley fault system, *NEHRP Technical Report, 01HQGR0019,* 41 pp.

Dixon, T., M. Miller, F. Farina, H. Wang, and D. Johnson (2000). Present-day motion of the Sierra Nevada block and some tectonic implications for the Basin and Range province, North American Cordillera, *Tectonics* **19,** 1–24.

Faulds, J. E., C. D. Henry, and N. H. Hinz (2005). Kinematics of the northern Walker Lane: An incipient transform fault along the Pacific–North American plate boundary, *Geology* **33,** 505–508.

Frankel, K. L., J. Dolan, R. Finkel, L. A. Owen, and J. S. Hoeft (2007). Spatial variations in slip rate along the Death Valley–Fish Lake Valley fault system determined from LiDAR topographic data and cosmogenic ¹⁰Be geochronology, *Geophys. Res. Lett.* **34,** 1–6.

Gold, R. D., and E. Cowgill (2011). Deriving fault-slip histories to test for secular variation in slip, with examples from the Kunlun and Awatere faults, *Earth Planet Sci. Lett.* **301,** 52–64.

Gosse, J. C., and F. M. Phillips (2001). Terrestrial in situ cosmogenic nuclides: Theory and application, *Quaternary Sci. Rev.* **20,** 1475–1560.

Grose, T. L. T. (1984). *Geologic map of the State Line Peak Quadrangle, Nevada–California,* Nevada Bureau of Mines and Geology, Map 82, scale 1:24,000.

Hammond, W. C., and W. Thatcher (2007). Crustal deformation across the Sierra Nevada, northern Walker Lane, Basin and Range transition, western United States measured with GPS 2000–2004, *J. Geophys. Res. B Solid Earth Planets* **112,** 1–26.

Hammond, W. C., G. Blewitt, and C. Kreemer (2011). Block Modeling of crustal deformation of the Northern Walker Lane and Basin and Range from GPS velocities, *J. Geophys. Res. B Solid Earth Planets* **116,** 1–28.

Hancock, G. S., R. S. Anderson, O. Chadwick, and R. Finkel (1999). Dating fluvial terraces with ¹⁰Be and ²⁶Al profiles: Application to the Wind River, Wyoming, *Geomorphology* **27,** 41–60.

Henry, C. D., J. E. Faulds, and C. M. dePolo (2007). Geometry and timing of strike-slip and normal faults in the northern Walker Lane, northwestern Nevada and northeastern California: Strain partitioning or sequential extensional and strike-slip deformation?, in *Exhumation Associated with Continental Strike-Slip Fault Systems,* S. M. Roeske, J. C. Sample, and D. A. Foster (Editors), Spec. Pap. Geol. Soc. Am., **434,** 59–79.

Hidy, A. J., J. C. Gosse, J. L. Pederson, J. P. Mattern, and R. C. Finkel (2010). A geologically constrained Monte Carlo approach to modeling exposure ages from profiles of cosmogenic nuclides: An example from Lees Ferry, Arizona, *Geochem. Geophys. Geosyst.* **11,** 1–10.

Hinz, N. H., J. E. Faulds, and C. D. Henry (2009). Tertiary volcanic stratigraphy and paleotopography of the Diamond and Fort Sage Mountains: Constraining slip along the Honey Lake fault zone in the northern Walker Lane, northeastern California and western Nevada, *Spec. Pap. Geol. Soc. Am.* **447,** 101–131.

Hubert-Ferrari, A., G. King, I. Manighetti, R. Armijo, B. Meyer, and P. Tapponnier (2003). Long-term elasticity in the continental lithosphere; modeling the Aden Ridge propagation and the Anatolian extrusion process, *Geophys. J. Int.* **153,** 111–132.

Klinger, Y., M. Etchebes, P. Tapponnier, and C. Narteau (2011). Characteristic slip for five great earthquakes along the Fuyun fault in China, *Nat. Geosci.* **4,** 389–392.

Knuepfer, P. L. K. (1992). Temporal Variations in Latest Quaternary Slip across the Australian-Pacific Plate Boundary, Northeastern South Island, New-Zealand, *Tectonics* **11,** 449–464.

Lal, D. (1991). Cosmic ray labeling of erosion surfaces: *in situ* nuclide production rates and erosion, *Earth Planet. Sci. Lett.* **104,** 424–439.

Le, K., J. Lee, L. A. Owen, and R. Finkel (2007). Late Quaternary slip rates along the Sierra Nevada frontal fault zone, California: Slip partitioning

across the western margin of the Eastern California Shear Zone–Basin and Range Province, *Bull. Geol. Soc. Am.* **119,** 240–256.

Lee, J., J. Garwood, D. F. Stockli, and J. Gosse (2009). Quaternary faulting in Queen Valley, California-Nevada: Implications for kinematics of fault-slip transfer in the eastern California shear zone–Walker Lane belt, *Bull. Geol. Soc. Am.* **121,** 599–614.

Nicol, A., J. Walsh, K. Berryman, and P. Villamor (2006). Interdependence of fault displacement rates and paleoearthquakes in an active rift, *Geology* **34,** 865–868.

Petersen, M. D., A. D. Frankel, S. C. Harmsen, C. S. Mueller, K. M. Haller, R. L. Wheeler, R. L. Wesson, Y. Zeng, O. S. Boyd, D. M. Perkins, N. Luco, E. H. Field, C. J. Wills, and K. S. Rukstales (2008). Documentation for the 2008 Update of the United States National Seismic Hazard Maps, *USGS Open-File Report-1128*, 61 pp.

Reimer, P., M. Baillie, E. Bard, A. Bayliss, J. Beck, P. Blackwell, C. B. Ramsey, C. Buck, G. Burr, R. Edwards, M. Friedrich, P. Grootes, T. Guilderson, I. Hajdas, T. Heaton, A. Hogg, K. Hughen, K. Kaiser, B. Kromer, F. McCormac, S. Manning, R. Reimer, D. Richards, J. Southon, S. Talamo, C. Turney, J. van der Plicht, and C. Weyhenmeyer (2009). IntCal09 and Marine09 radiocarbon age calibration curves, 0–50,000 years cal BP, *Radiocarbon* **51,** 1111–1150.

Repka, J. L., R. S. Anderson, and R. C. Finkel (1997). Cosmogenic dating of fluvial terraces, Fremont River, Utah, *Earth Planet. Sci. Lett.* **152,** 59–73.

Stone, J. (2000). Air pressure and cosmogenic isotope production, *J. Geophys. Res.* **105,** 23,753–23,759.

Thatcher, W. (2003). GPS constraints on the kinematics of continental deformation, *Int. Geol. Rev.* **45,** 191–212.

Thatcher, W., G. R. Foulger, B. R. Julia, J. Svarc, E. Quilty, and G. W. Bawden (1999). Present-day deformation across the Basin and Range Province, western United States, *Science* **283,** 1714–1718.

Turner, R., R. D. Koehler, R. W. Briggs, and S. G. Wesnousky (2008). Paleoseismic and Slip-Rate Observations along the Honey Lake Fault Zone, Northeastern California, USA, *Bull. Seismol. Soc. Am.* **98,** 1730–1736.

U.S. Geological Survey, Nevada Bureau of Mines and Geology, and California Geological Survey (2006). Quaternary fault and fold database for the United States, USGS website: http://earthquakes.usgs.gov/regional/qfaults/ (last accessed October 2011).

Weldon, R. J., K. M. Scharer, T. E. Fumal, and G. P. Biasi (2004). Wrightwood and the earthquake cycle; what a long recurrence record tells us about how faults work, *GSA Today* **14,** 4–10.

Wesnousky, S. G. (2005). Active faulting in the Walker Lane, *Tectonics* **24,** 1–35.

Wesnousky, S. G., and M. Caffee (2011). Range-bounding normal fault of Smith Valley, Nevada: Limits on age of last surface-rupture earthquake and late Pleistocene rate of displacement, *Bull. Seismol. Soc. Am.* **101,** 1431–1437.

Wills, C. J. (1990). Honey Lake and related faults, Lassen County: California Division of Mines and Geology, *Fault Evaluation Report 214*, scale 1:24,000, 17 pp.

Wills, C. J., and G. Borchardt (1993). Holocene slip rate and earthquake recurrence on the Honey Lake fault zone, northeastern California, *Geology* **21,** 853–856.

Zreda, M., and F. M. Phillips (1994). Surface exposure dating by cosmogenic chlorine-36 accumulation, in *Dating in Exposed and Surface Contexts*, C. Beck (Editor), University of New Mexico Press, 161–183.

Appendix A

LiDAR Data

A critical source of data for our investigation was airborne LiDAR data, which were collected in October 2011 at an average elevation of 400 m above mean terrain. Flight lines overlapped by 55%, the maximum scan angle was $\pm 20°$ from nadir, and the resultant data have 15–17 raw returns per square meter. Vertical uncertainties in the LiDAR and root mean square (rms) errors ranged from 4–7 cm across the survey area. The vendor classified the point cloud data and delivered a bare earth digital-elevation model with a grid size of 0.25 m, created using a triangulation approach with the Terrascan™[1] software package.

Appendix B

Qo2 Deposit

Two hand-dug pits exposed a debris-flow-dominated fan facies with minor fluvial beds. Pit1SW was excavated into the southern/upslope Qo2 deposit, 86 m south of the fault (Figs. 2 and 6). The pit had a maximum depth of 100 cm below the Qo2 surface (Fig. 6a,b). Pit2NE was a small exploratory excavation into the northern/downslope lobe of the Qo2 deposit, 29 m north of the fault (Fig. 2). This pit reached a depth of 40 cm below the surface, and we used it to compare soil development in the upper portion of the Qo2 deposit on opposite sides of the fault.

The excavations revealed a capping 2–5 cm thick A_1 horizon with pervasive root materials set in a silty matrix with a burn horizon. From 5–20-cm depth below the surface, there is a silt-dominated, matrix-supported A_2 mollic soil interspersed with weathered gravels <10 cm in diameter. We interpret this horizon to result from a combination of eolian silt input (derived from the Honey Lake basin source), combined with dynamic soil-formation processes such as overland sheet wash, bioturbation, and freeze-thaw. From 20–30 cm below the surface we observed a transitional AB horizon that is silt dominated with minor clay and is interspersed with weathered clasts. From 30 to 90 cm below the trench surface, a weathered version of the original Qo2 deposit is preserved. This well-indurated horizon includes weathered granite clasts, intact volcanic boulders, and a silty clay matrix with minor sand. We classify this horizon as B_{t1}, composed of sandy clay loam. The deepest part of the deposit was observed only in the basal part of Pit1SW from 90 to 100 cm below the surface. At this depth, the deposit is well cemented and is grayer in color than the above B_{t1} soil. We define this basal unit as a B_{t2} horizon. We were unable to excavate to the depth of unmodified parent material (Qo2). Similar stratigraphic layers and levels of soil development observed in the upper 40 cm of both pits support our inference that the mapped Qo2 fan lobes are coeval. Furthermore, the distinct presence of clays and the thickness of the B soils (>1 m below fan surface) are evidence of a significant interval of weathering and soil development since deposition of the Qo2 deposit.

---

[1]Any use of trade, firm, or product names is for descriptive purposes only and does not imply endorsement by the U.S. government.

Appendix C

^{10}Be Analysis

Amalgamated sandy gravel samples for cosmogenic ^{10}Be analysis were collected at depths of 37, 49, 74, and 86 cm below the fan surface within zones ± 3 cm from the aforementioned depths. A mixed zone visible below the covering silts was distinct from the unmixed sediments, which exhibited weak bedding and structure. All samples were collected below the mixed zone within the Qo2 boulder gravel. The samples were washed and sieved to cull the 350–500 μm and 500–1000 μm sand fractions for analysis. Samples underwent quartz purification and isotope extraction at the Cosmogenic Nuclide Geochronology Laboratory at the Georgia Institute of Technology. Accelerator Mass Spectrometry (AMS) measurements were conducted at the Center for Accelerator Mass Spectrometry (CAMS) at Lawrence Livermore National Laboratory (LLNL) (Table 1).

We used a Monte Carlo depth-profile calculator (Hidy *et al.*, 2010, version 2.1) to calculate the most probable exposure duration, erosion (or aggradation) rate, and inherited nuclide concentration. Net erosion of −30 cm (i.e., aggradation of 30 cm) to 20 cm was constrained from field observations and was modeled assuming stochastic uniform probability because we lack independent constraints, other than minimum and maximum erosional bounds to favor a Gaussian, triangular, or other shaped distribution. A variable density was approximated with conservative uncertainties for the profile based on the grain size and texture observed (A1 1.4 ± 0.3, A2 1.4 ± 0.3, AB 1.5 ± 0.3, Bt 2 ± 0.2, and Bt 22.1 ± 0.2 g cm^{-3}). Ages were calculated using a site-production rate (13.1 atom g^{-1} yr^{-1}) scaled using the Lifton time-varying production rate provided in the CRONUS-Calculator (Balco *et al.*, 2008). Note, this production rate or depth-profile calculator does not use the new CRONUS-Earth ^{10}Be production rate of 4.3 atom g^{-1} yr^{-1} for sea level–high latitude and the effect of erosion (or aggradation) is calculated assuming a constant rate against the time-varying site production rate. The ^{10}Be age in this manuscript will likely be on the order of 10% younger than an age calculated with the unpublished CRONUS-Earth rate and a coupled erosion-paleointensity variation computation.

The ^{10}Be concentration of the four samples decrease with depth and indicate that post-depositional vertical mixing was negligible and that the inherited concentration was similarly small in each of the amalgamated sand samples (Fig. 7c). The solutions for age, erosion rate, and inheritance concentrations are provided in Table 2. The ^{10}Be depth profile is based on all four samples. The black curve shown in Figure 7c is the one that corresponds with the lowest χ^2 of 1,000,000 possible curves. The ^{10}Be concentration error bars are at $2 - \sigma$ uncertainty in the total error (i.e., calculated using the AMS precision and a small (2% at 1σ) chemistry error), which largely reflects uncertainty in the carrier concentration. The bulk density used (Fig. 7d) is the cumulative bulk density from the measurement of density throughout the profile. The probability density functions and cumulative-distribution functions (Fig. 7e) for the depositional age fan assumes a simple 1-stage deposition followed by a range of surface erosion (up to 20 cm) and aggradation of eolian sediment (up to 30 cm) based on geomorphic and soils constraints at the surface. A slightly erosive history with negligible inherited concentration yield the Bayesian most probable age of $41.4^{+10.0}_{-4.8}$ ka. Our sensitivity tests indicate that erosion is the largest source of error in the fan age.

Appendix D

^{36}Cl Dating of Basaltic Boulders

At the Fort Sage alluvial-fan site boulders on the Qo2 surface with diameters ≥ 1 m are prevalent and included three dominant lithologies: porphyritic basalt, rhyolite tuff, and granodiorite. The basalt boulders, which are the most abundant at the site, protrude ≥ 1 m above the fan surface, and they show more limited evidence of weathering compared to boulders of other lithologies. First, we sought to satisfy the criteria of sampling from the original surface in question, Qo2. We sought boulders that appeared to be located on sections of the Qo2 surface that appeared to be minimally eroded and incised. Second, to satisfy the criteria of boulder stability, we sought boulders with wide (> 2 m) bases and significantly developed varnish, which served as an indication that the boulders have remained stable since deposition. Finally, to satisfy geometric constraints, we sought boulders with flat surfaces with evidence for minimal weathering and alteration. In the following section, we present a description of the boulders. In the absence of high boulders with sufficient quartz for ^{10}Be analysis, we selected boulders for ^{36}Cl exposure dating (Zreda and Phillips, 1994).

Samples were chipped from the upper 2–3 cm of the flat tops of the boulder surfaces. Masses of ∼100 g of the samples were dissolved to extract Cl using standard procedures (Zreda and Phillips, 1994) at Dalhousie Geochronology Centre. AMS measurement of the ^{36}Cl/Cl and the ^{35}Cl/^{36}Cl ratios were made at PRIME Lab at Purdue University (Table 3). Elemental chemistry was measured using X-Ray Fluorescence Spectrometry (XRF) and ICP-MS by SGS Minerals, Canada (Table 4). The online Cronus ^{36}Cl Exposure Age calculator was used to calculate boulder ages.

V01 (176.9 ± 24.1 ka [2σ], Fig. 6b)—the reddish, basaltic V01 boulder sits 0.7 m above the fan surface, north of the Warm Springs Valley fault system. The boulder displays pervasive, shallow (< 3–5 cm deep) cracks spaced 25–35 cm apart. The boulder is very well indurated and was extremely difficult to sample in coherent fragments. All samples came from the upper 2 to 2.5 cm of the boulder surface and were collected away from cracks in the boulder.

V04 (55.7 ± 9.2 ka [2σ], Fig. 6c)—the reddish basaltic V04 boulder protrudes 0.7–0.8 m above the fan surface, south of the WSVFS. A weathering line on the southern face of the boulder indicates it may have been previously covered by up to 20 cm above the current fan surface by silts and that material may have been more recently removed. Sample material was collected from a gently south-sloping surface with an orientation of 102, 16S and away from regions of apparent exfoliation.

V06 (130.3 ± 16.7 ka [2σ], Fig. 6d)—the reddish V06 boulder sits only 20–30 cm (upslope) and 70 cm (downslope) above the fan surface and has a diameter of ~3 m. It is located south of the WSVFS. Despite its lower-than-ideal height above the fan surface, the large diameter indicates long-term stability (e.g., has not rolled). Although the fan surface has clearly experienced burial by eolian silts, the local climate makes it unlikely that snow has significantly buried the boulder surface, and we know of no thick tephra deposits that would have persisted on the fan surface in the late Pleistocene. Furthermore, the boulder is extremely well indurated.

The presence of inherited ^{36}Cl yields an anomalously old age for the boulder, and therefore the deposit (Gosse and Phillips, 2001 and references therein). Given the small number of boulders preserved on the Qo2 surface with limited evidence of weathering, we interpret the significant scatter in ages to reflect inheritance of ^{36}Cl from previous exposure. Thus, we estimate that the lowest of the three ages probably represents the closest estimate of the age of the fan.

Geologic Hazards Science Center
U.S. Geological Survey
1711 Illinois Street
Golden, Colorado 80401
rgold@usgs.gov
    (R.G., R.B., A.C.)

Nevada Bureau of Mines and Geology
Mail Stop 178
University of Nevada
Reno, Nevada 89557
    (C.d.)

Department of Earth Sciences
Dalhousie University
1459 Oxford Street
Halifax, Nova Scotia B3H 4R2, Canada
    (J.G.)